Nano Research

Open Access

Research Article

Decoding ripple formation in single-layer transition metal chalcogenide lateral heterojunctions towards novel optoelectronic properties

Haitao Yu[1,2], Mingzi Sun[3], Xiao Wu[1,2], Zhiguo Xing[1,2], Jiahao Kou[1,2], Shipeng Liang[1,2], Bolong Huang[1,2,3,4] ✉, and Zhong Lin Wang[1,2,5] ✉

[1] *CAS Center for Excellence in Nanoscience, Beijing Institute of Nanoenergy and Nanosystems, Chinese Academy of Sciences, Beijing 100083, China*
[2] *School of Nanoscience and Technology, University of Chinese Academy of Sciences, Beijing 100049, China*
[3] *Department of Applied Biology and Chemical Technology, The Hong Kong Polytechnic University, Hong Kong 999077, China*
[4] *Research Centre for Carbon-Strategic Catalysis, The Hong Kong Polytechnic University, Hong Kong 999077, China*
[5] *School of Materials Science and Engineering, Georgia Institute of Technology, Atlanta, Georgia 30332, USA*

Cite this article: *Nano Research*, **2025**, *18*, 94907091. https://doi.org/10.26599/NR.2025.94907091

ABSTRACT: For the ultrathin two-dimensional (2D) materials and lateral heterojunction, the formation of unstable but elastic ripples is commonly observed but is rarely studied, especially their correlations with different material properties. To fill the knowledge gap in this field, this work systematically explores transition metal dichalcogenides (TMDCs) in a single component and lateral heterojunction with a series of ripple structures. The ripple formation energy is quantitatively classified into the initial elastic strain stage and fracture threshold stage based on Fermi-like distribution. Electronic structures reveal that the formation of ripples is accompanied by electron accumulations from flat surfaces to ripples. By comparing the unilateral, decaying, and bilateral ripples in 2D lateral heterojunction, we confirm that Fermi-like distribution is still valid regardless of the shape of the ripples, where the thermodynamic and electronic properties are modulated by ripples-induced uneven strain. The main features of optical properties are not affected while the sensitivity to ripple-induced strains is distinguished. More importantly, the phonon properties further demonstrate the potential of ripples in promoting thermal conductivity, which are strongly correlated with the optical branch of anion vibrations. This work provides important theoretical guidance for the design and optimization of high-performance optoelectronic devices based on TMDC heterojunctions.

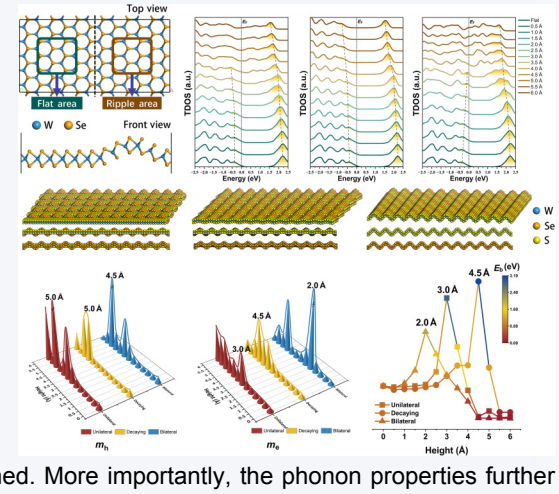

KEYWORDS: transition metal calcogenide, lateral heterojunctions, ripples, optoelectronic properties, two-dimensional (2D) materials

1 Introduction

Two-dimensional (2D) materials are an emerging field that has become a hot field of scientific research and technological innovation. In particular, the successful separation of monolayer graphene by mechanical exfoliation in 2004 has opened a new era in the study of 2D materials [1]. Since then, lots of different types of 2D materials have appeared, and the transition metal dichalcogenides (TMDCs) is one of the most studied ones due to their unique structures with high flexibility. Compared with graphene, black phosphorus [2], and mxenes [3], TMDCs have tunable electronic structures, higher mechanical properties, excellent stability, and more potential for large-scale production, integration, and application [4–8].

To optimize the properties of 2D materials, combinations of 2D materials with different physical and chemical properties become a promising approach to building up 2D heterojunctions with novel

Received: October 5, 2024; **Revised:** October 21, 2024
Accepted: October 22, 2024

✉Address correspondence to Bolong Huang, bhuang@polyu.edu.hk, huangbolong@binn.cas.cn; Zhong Lin Wang, zhong.wang@mse.gatech.edu

interface properties [9, 10]. Specifically, the heterojunctions of TMDCs, such as tungsten disulfide (WS_2) and tungsten diselenide (WSe_2), have garnered considerable attention due to their distinct electronic and optical properties. There is a discrepancy in the lattice constants of these materials; the lattice constant of WS_2 is 3.147 Å, whereas that of WSe_2 is 3.282 Å, resulting in approximately 4% lattice mismatch between them. This lattice mismatch, confirmed through previous experimental and simulation studies, is the primary cause of non-uniform strain at the heterojunction interface, which in turn spontaneously forms ripples or wrinkles on the material surface [11–13]. By interface engineering, the regulation of electronic behaviors, and improvements of mechanical stability are achieved. More importantly, the 2D heterojunctions also produce new physical phenomena such as the quantum Hall effect, superconductivity, and magnetism, enabling them to be promising candidates in the fields of optoelectronic devices, energy storage and conversion, and flexible electronics [14–17]. For 2D heterojunctions, the reduction of thickness, the interactions between heterogeneous materials, and interface morphology significantly change their electronic structure. During the synthesis of 2D heterojunction materials, it is always observed that the surface will spontaneously form ripples or wrinkles due to the non-uniform strain inside the material. Xie et al. [18, 19] observed the existence of out-of-plane periodic ripples along the heterogeneous interface in WS_2/WSe_2 coherent superlattices by atomic force microscopy (AFM). At the same time, Tian et al. [20] observed by aberration-corrected scanning transmission electron microscopy (AC-STEM), and successfully constructed a monolayer MoS_2/WSe_2 heterojunction model by first-principles methods. Park et al. reveal the formed superlattices with engineered strain within WS_2/WSe_2 heterostructures, which flexibly modulate the electronic properties [21]. Such ripple geometry leads to unique stretchability, compressibility, and bendability in the heterojunctions [22].

Currently, the views on the formation of ripples in heterojunctions are (1) lattice mismatch caused by lattice constant difference between heterojunctions; (2) inconsistency of thermal expansion coefficient between heterojunctions; and (3) internal stress caused by chemical composition difference. Han et al. [12] reported the dislocations and ripples in the WS_2/WSe_2 lateral heterojunction array by the electron microscope pixel array detector (EMPAD). They proposed that the in-plane strain caused by the different lattice constants was released mainly through out-of-plane ripples. The difference in thermal expansion coefficient also leads to a thermal mismatch between 2D materials and the substrate, which limits the epitaxial growth of 2D heterogeneous materials [23, 24]. In addition, the anion coupling between the components of the heterojunction causes charge perturbation, resulting in the formation of ripples at the WS_2/WSe_2 lateral heterojunction interface [25]. All these works have revealed the strong interactions in 2D heterojunction structures, which are important factors in determining the optoelectronic properties.

For the synthesis of heterojunctions, scientists have often observed the sharp atomic interfaces at the heterostructures of TMDCs, which can be considered as ripples [26, 27]. Many recent studies have reported the application potential of ripples, especially in lateral heterojunctions. Zhang et al. [28] found that the lattice mismatch strain in the WSe_2/MoS_2 heterojunction changes the band alignment from type I to type II band alignment at the interface. Meanwhile, Ghosh et al. [29] realized the exciton manipulation to enhance the photoelectrochemical hydrogen evolution reaction (HER) on the 2D materials. They have confirmed that localized excitons at the rippled structures with uneven strain exhibit a decreased exciton binding energy to realize the more efficient generation of carriers under light. These studies demonstrate that the electronic modulation of heterojunctions by rippled structures can be applied to nano-optoelectronics, sensing, and catalysis. Li et al. [30] found that the lattice mismatch at the interface would significantly affect the photoluminescence intensity by two-step epitaxial growth of lateral WSe_2-MoS_2 heterojunction. Zhou et al. [13] found that the misfit dislocations at the WS_2/WSe_2 heterojunction interface drive the growth of quantum well arrays, indicating that the structure is transformed into a "channel" of conductive nanoribbons by n-type doping. The above works show that the rippled structure caused by uneven strain has great potential in modulating the properties of the heterojunctions. The d-p-d orbital couplings within the heterojunction interface between d-orbitals of anions (TMs) and p-orbitals of cations (S/Se) are sensitive to the strain, which controls the properties of the TMDC heterojunctions [31, 32]. However, detailed explorations into the morphology of the ripples in the 2D TMDCs and the corresponding heterojunctions are still needed. Therefore, systematic and in-depth theoretical explorations from the atomic views are significant in supplying critical insights into the formation and modulations of heterojunctions.

In this work, we have carried out a systematic theoretical study to explore the correlations of the ripple morphology with the band structure, electronic density of states, and optical properties of the heterojunctions. In this study, by applying strain on single-layer TMDCs, a two-stage structural energy evolution trend is proposed, which quantifies the relationship between ripple structure and energy. Through electronic structure analysis, we found that strain increases the free carrier concentration and induces electron transfer from the Fermi level (E_F) to ripple top regions. In addition, among three different ripple morphologies including the unilateral, decaying, and bilateral ripples (U-Ripple, D-Ripple, and B-Ripple), the D-Ripple with the lowest strain shows the slowest bandgap and the mildest change in electronic structures and optical properties. The phonon density of states (DOS) indicates that the optical branch is mainly dominated by the d-p-d orbital couplings through S/Se atoms, which are highly sensitive to the ripple strain. This study will provide an important theoretical reference to reveal the essential role of strain in 2D materials and heterojunctions, which further facilitates the optimizations of performance and broadening the application of two-dimensional TMDCs.

2 Results and discussion

To reveal the influences of the ripple structures on different properties of TMDCs, we first calculate the energy evolutions of monolayer MoS_2, WS_2, and WSe_2 with the ripple structures in both armchair and zigzag directions (Fig. 1(a) and Fig. S1 in Electronic Supplementary Material (ESM)). At the initial formation of the ripple with the height from 0–1 Å, the increasing trend of energy is relatively slow, where the ripple-induced instability is alleviated by the overall TMDC structures. As the ripple height further increases and exceeds 1.5 Å, the energy shows a fast-increasing trend with much higher instability. When the ripples break through the elastic strain stage, the increasing rate of energy reduces. After reaching the fracture threshold height of the ripple, the energy evolutions become flattened and relatively stable. The overall energy evolutions induced by ripples in TMDCs all display “S” trends. Since the energy evolutions become irregular with the further increasing

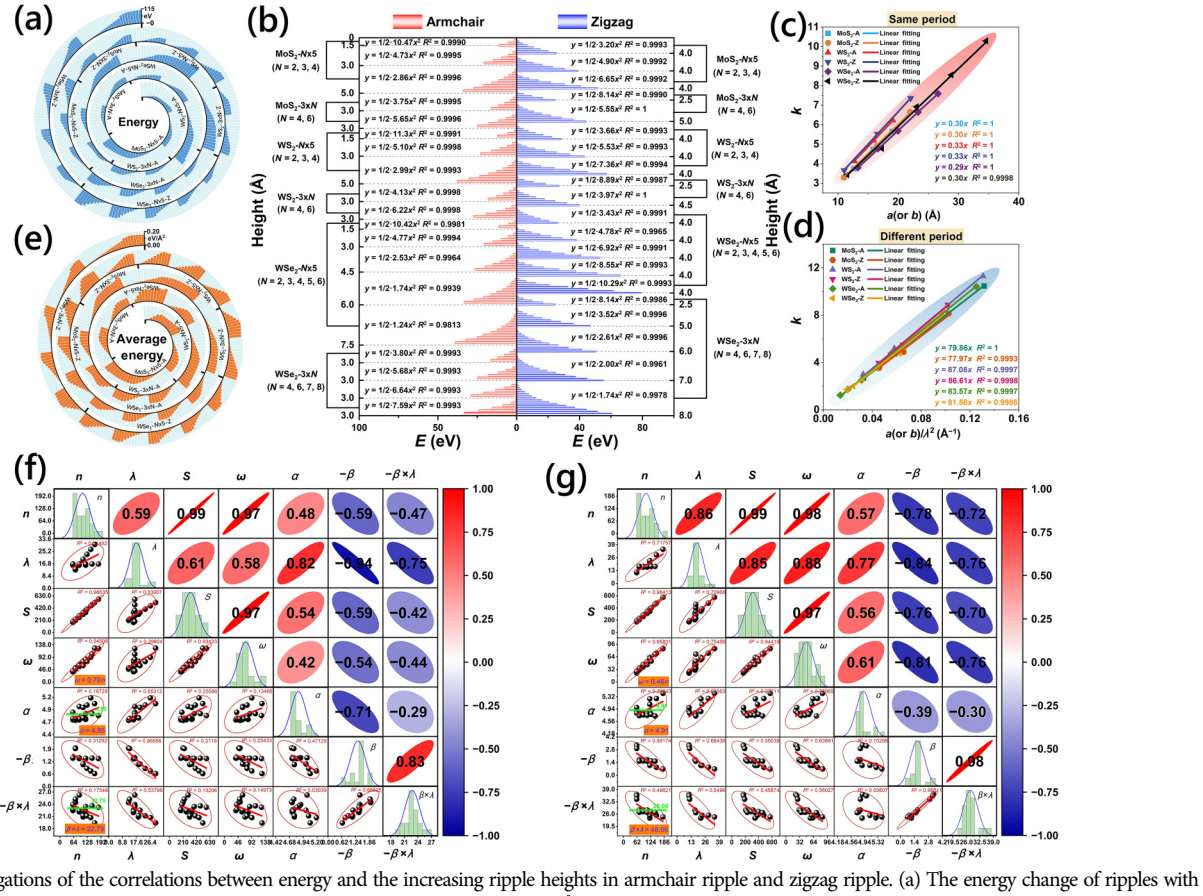

Figure 1 Investigations of the correlations between energy and the increasing ripple heights in armchair ripple and zigzag ripple. (a) The energy change of ripples with different heights in and 3 × *N* supercells. The increase step of the ripple height is 0.5 Å. (b) The numerical fitting of the energy with different ripple structures. The correlation between the quadratic fitting parameter *k* and the lattice parameter *a* or *b* divided by λ^2 in the (c) same period and (d) different periods in (b). λ is the ripple period. (e) The average energy of the ripple structures based on the rippled surface area. The correlations among different energy fitting parameters ω, α, β, $\beta \times \lambda$, *n*, λ, *S* in the (f) armchair and (g) zigzag ripples. *n* is the number of atoms of each ripple; λ is the periods of ripples; *S* is the surface area of the ripples.

ripple heights, we mainly focus on two ripple stages: 1) the elastic strain stage and 2) the fracture threshold.

For the elastic strain stage, the ripples undergo elastic deformation, and the ripple strain ε can be derived based on the following equation, which is regardless of the ripple shape used for model building (Eq. (1)).

$$\varepsilon = \frac{\pi^2 S\delta}{(1-\nu^2)\lambda^2} \tag{1}$$

In Eq. (1), *S* is the thickness of the monolayer, δ is the ripple height, ν is the Poisson's ratio of TMDCs, and λ is the ripple period.

The stress represents a deforming force applied to an object while the corresponding deformation of the material induced by the stress is the strain. According to the relationship between stress and strain, we derive the following equation (Eq. (2))

$$\sigma = B \times \varepsilon = \frac{B\pi^2 hH}{(1-\nu^2)\lambda^2} \tag{2}$$

In the above equation, σ is the stress of TMDCs ripples, *B* is the bending modulus of the material, and *H* is the ripple height of TMDCs. According to Eqs. (1) and (2), the stress is linearly related to the ripple height, so the energy *E* of the first stage of the ripple can be obtained as follows (Eq.(3))

$$E = \frac{1}{2} \times a\,(\text{or } b) \times \sigma = \frac{\frac{1}{2}\pi^2 hE_{\text{bending}}}{1-\nu^2} \times b \times H^2 \tag{3}$$

where *a* and *b* are the length and width of the ripples, respectively, and *H* is the rippled height. By applying *a* or *b* in the equation, we obtain the energy of the zigzag chair and armchair ripples, respectively. It can be seen from Eq. (3) that the relationship between the energy *E* and the ripple height at the elastic strain stage is a quadratic function, which satisfies the elastic strain relationship as well as the first-order harmonic vibration mode. Since the sizes of TMDCs have a great influence on the flexural modulus of the materials, the E_{bending} will be further studied and optimized in future works.

According to the first-order harmonic vibration mode, the elastic potential energy is $E = \frac{1}{2}kx^2$ (where *k* is the elastic coefficient, and *x* corresponds to the ripple height *H* in our work). Based on the above derivations, we apply the quadratic function form to correlate the energy and ripple height in the elastic strain stage (Fig. 1(b)). Notably, all the fittings display high R^2 values, supporting the strong correlation between the energy and the elastic strain induced by the ripples. With further investigations of the elastic coefficient, we have identified that *k* is proportional to the ripple parameters (length of ripples *a* for zigzag ripple and width of the ripples *b* for armchair ripple) when the ripple period is the same (Fig. S2(a) in the ESM).

When the ripple period changes, k is proportional to the reciprocal of the square of the ripple period $\frac{1}{\lambda^2}$ (Fig. S2(b) in the ESM). Accordingly, we have fitted k with $\frac{a}{\lambda^2}$ (zigzag ripple) and $\frac{b}{\lambda^2}$ (armchair ripple), leading to the $k = 84.40\frac{a}{\lambda^2}$ (armchair ripple of WSe_2) (Fig. 1(c)) and $k = 81.70\frac{a}{\lambda^2}$ (zigzag ripple of WSe_2) (Fig. 1(d)), respectively, where the constants are obtained based on the average data of the same and different periods. With these fittings, the energy evolutions of the ripple structures in the elastic strain stage are expressed below Eq. (4)

$$E = \frac{1}{2} \times 84.40\frac{a\,(\text{or } b)}{\lambda^2} \times H^2 \tag{4}$$

By comparing Eq. (3) with Eq. (4), we confirm that the energy of the first stage is indeed the elastic strain stage. Based on the structural energy changes, the energy evolutions become flattened and relatively stable after reaching the fractured threshold height of the ripple, which is considered as the second stage. For the second stage of fracture threshold, since the overall energy trend is similar to the most probable distribution of particles in the Fermi system $N = \sum_l \frac{\omega_l}{e^{\alpha+\beta\times\varepsilon_l}+1}$ (where l is commonly used to denote the energy level index of a quantum state. This index l serves to differentiate the various energy levels within a system, with each specific energy level corresponding to a unique energy value and its corresponding degeneracy ω_l), we propose the Fermi-like distribution function for our work as shown below Eq. (5)

$$E = \frac{\omega}{e^{\alpha+\beta\times H}+1} \tag{5}$$

where E is the energy of monolayer TMDCs with ripples, H is the height of the ripple, and ω, α, β are the parameters of the Fermi-like distribution function for energy. Based on our function fitting of energy increase, the specific values of each parameter are shown in Table S1 in the ESM. With such a correlation, the corresponding influences of the ripples on 2D materials are quantified to guide the suitable strain engineering for reaching the balance between property optimizations and stability.

We analyze the correlation of the parameters (ω, α, β) of the Fermi-like distribution function of energy to investigate the potential affecting properties to the energy changes of rippled structures (Figs. 1(e) and 1(f)). It is noted that the energy distributions to different parameters are also different in the armchair and zigzag directions, where we apply the Pearson correlation coefficient (P) as the indicator to measure the linear correlation among different parameters [33]. The P values range from −1 to 1, which indicates both positive and negative correlations between the factors, which is different from the coefficient of determination R^2. The P between the parameter ω and the atomic number n are 0.98 and 0.97 for armchair (Fig. 1(e)) and zigzag ripple (Fig. 1(f)), respectively, indicating a strong positive correlation. The corresponding fitting reaches the $\omega = 0.46n$ (R^2 = 0.9583) and $\omega = 0.70n$ (R^2 = 0.9451) for armchair and zigzag ripple, respectively, where the difference of ω values in the two directions originates from the directionality of the tensile properties of the material, supporting our previous research that the rippled strain is anisotropic [34]. On the other side, the coefficient P between parameter α and each influencing factor display very limited regularity, and they are concentrated in the range of 4.7–5.2 (armchair) and 4.7–5.3 (zigzag), respectively. After fitting, the corresponding α parameter in our proposed Fermi-like distribution function of energy is 4.91 for the armchair ripples and 4.85 for zigzag ripples, which still proves the anisotropic properties of TMDCs. In addition, the correlations between the parameter β and other influencing factors result in a slightly higher P than that of the α parameter. In comparison, the P distributions of $\beta \times \lambda$ in both directions are more concentrated, leading to the $\beta \times \lambda$ equal to 28.06 for armchair ripples and 22.75 for zigzag ripples after fitting. Therefore, the proposed "Fermi-like distribution function" of energy expressions of the second stage ripples are shown below Eqs. (6) and (7)

$$\text{Armchair ripple}: E = \frac{0.46 \times n}{e^{4.91-\frac{28.06}{\lambda}\times H}+1} \tag{6}$$

$$\text{Zigzag ripple}: E = \frac{0.70 \times n}{e^{4.85-\frac{22.75}{\lambda}\times H}+1} \tag{7}$$

The average energy of the ripples also shows a Fermi-like distribution, where the average energy decreases when the ripple height for the fracture threshold increases (Fig. 1(g)). This is because the threshold reaches the height of the rippled fracture. As the ripple heights of TMDCs continuously increase, the surface area also keeps increasing until the fracture, which interrupts the further energy increase due to the evident structural deformation. This further results in the reductions of average energy. When the ripple period changes at the same ripple height, the average energies display an opposite trend to the period. When the ripple period is fixed, the average energies of TMDCs at the same ripple height are independent of the ripple sizes. Based on the above discussions, we have derived the corresponding correlation expression for the first elastic strain stage and the second Fermi-like distribution stage, which quantitatively describes the energy evolution trends for both armchair and zigzag ripples, enriching the theoretical explorations of advanced functional TMDCs.

Since the electronic distributions will be modulated with the strain in materials [4, 35, 36], we have established a 6 × 5 WSe_2 ripple structure including 180 atoms with combinations of flat area and ripple area to reveal the electronic modulations induced by the uneven strain distributions in different regions of TMDCs (Fig. 2(a)). In particular, we choose the central areas of both flat area and ripple area to demonstrate the detailed electronic structures to distinguish the strain effect. The electronic structures of these combined rippled structures are demonstrated by the overall structure total density of states (TDOSs), which has remained similar when the ripple height is between 0–1.5 Å (Fig. 2(b)). This further confirms that the TMDC structure is able to alleviate the instability induced by minor ripples (< 1.5 Å) without affecting the overall properties. As the ripple height reaches 2.0 Å, both the conduction band minimum (CBM) and valence band maximum (VBM) begin to redshift, and become stable for VBM and CBM when the ripple height increases to 4.5 Å. The corresponding band structures also prove that the TMDCs become metallic-like when the ripple height reaches 5.5 Å (Fig. 2(c)). For the flat area, the TDOSs changes are much smaller than the ripple area, where W-5d orbitals exhibit higher portions than the Se-4p orbitals near the Fermi level (Fig. S3(a) in the ESM). This reveals that the W-5d orbitals near the E_F are more sensitive to the strain induced by the ripples in the nearby regions. Notably, from the ripple height of 2.5 Å, the change of W-5d and Se-4p orbitals show a parallel redshift trend. In contrast, the TDOSs

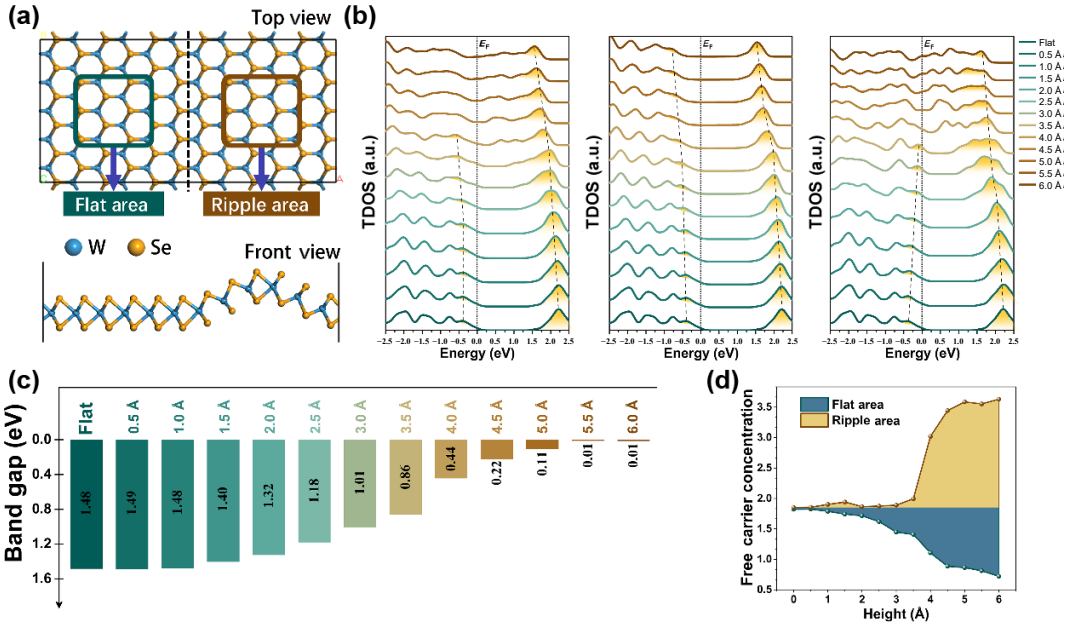

Figure 2 Free charge carrier transfer analysis in strain induced by ripples. (a) The demonstration of WSe_2 ripple structure in a 6 × 5 supercell, in which the left half is the flat area, and the right half is the ripple area. (b) The overall TDOSs and TDOSs of the flat area and ripple area in (a). (c) The bandgap evolution with increasing ripple heights. (d) The estimated concentrations of free charge carriers near E_F of both the flat and ripple areas.

changes of the ripple area are much more intensive (Fig. 2(b)). The VBM and CBM start the blueshift and redshift, respectively at the ripple height of 2.5 Å. The band gaps disappear at the ripple height of 4.5 Å and the electron density becomes higher near the E_F, especially the 5d orbitals from W sites (Fig. S3(b) in the ESM). Accordingly, the estimation of free carriers is performed by the projected partial density of states (PDOSs) near the E_F within the range from −1.0 to 1.0 eV (Fig. 2(d)). It can be found that the free carrier concentrations in the flat area decrease gradually while the ripple area has a great improvement of free carrier concentrations at the ripple height of 3.5 Å. In order to explore the reason, we further demonstrate the 3D contour plot of the electronic distributions near the E_F, where strong d-p-d orbital coupling between W-5d and Se-4p orbitals (Fig. S3(c) in the ESM). To further visualize the electronic distributions near VBM and CBM, we plot the evolutions of the highest occupied and lowest unoccupied orbitals (HOMO and LUMO). Within the range of 1.5 Å for the ripple height, the HOMO and LUMO are evenly distributed on both sides, which is consistent with the TDOSs trend, indicating that the electronic structures are not affected by the minor ripples. From the ripple height of 2.0 Å, the HOMO/LUMO gradually disappear on the flat area and shifts to the ripple area, revealing that the ripples start to dominate electronic structures. Combined with the analysis of free carrier concentration in PDOSs, it is concluded that with the increase of ripple height, the electrons near E_F gradually transfer from the flat to the ripple area. These results confirm that the uneven strain distributions induced by the local ripples drive electron transfer between the ripple and flat area, supporting that ripples are able to realize different types of charge carrier transfers in 2D materials. Different from TMDCs, ripples in other 2D materials such as graphene or hBN are proven to be beneficial for proton transfer by experiments [37, 38].

As discussed in previous sections, the free carriers transfer with the strain gradient, which is critical for the lateral heterojunction. Owing to the mismatch of the lattice constants between two materials, the ripples are often formed at the interface with the appearance of uneven strain distributions. To further reveal the influences of ripples in the lateral structures, we have designed a series of WS_2/WSe_2 heterojunctions (Figs. 3(a)–3(c) and Fig. S4(a) in the ESM). Since the lattice constant of WSe_2 is larger than that of WS_2, it is expected that the Ripples will form on the WSe_2 side due to the stronger compression strain, which also affects WSe_2 region close to the heterojunction. Accordingly, we have constructed three types of heterojunction structures including U-Ripple, D-Ripple and B-Ripple. U-Ripple: In the heterojunction, the WSe_2 side forms a wavy structure while the WS_2 side remains flat (Fig. 3(a)). D-Ripple: The ripple is gradually transferred from the WSe_2 to the WS_2 side in the heterojunction, and the ripple height is gradually attenuated (Fig. 3(b)). B-Ripple: The ripples at the same height are formed on both sides of the heterojunction (Fig. 3(c)). The model functions of these three heterojunctions are as follows (Eqs. (8)-(10))

$$\text{U-Ripple}: \quad z = A\cos\left(\frac{2\pi y}{\lambda}\right) \tag{8}$$

$$\text{D-Ripple}: \quad z = \frac{2A}{1+e^{\beta x}}\cos\left(\frac{2\pi y}{\lambda}\right) \tag{9}$$

$$\text{B-Ripple}: \quad z = A\cos\left(\frac{2\pi y}{\lambda}\right) \tag{10}$$

where A is the amplitude of the equation, and the height of the ripple is adjusted by the amplitude; λ is the ripple period; β is the attenuation coefficient, which has been set to −0.05 in this work.

We have conducted a systematic statistical analysis of the ripple strain in heterojunctions, with particular attention to the changes in bond length and the occurrence of bond rupture (Fig. S5 in the ESM). Our study found that within the ripple height range of 0 to 2.0 Å, the bond lengths in the three types of heterojunctions exhibited minimal variation and few bond ruptures. As the ripple height further increased, strain began to cause fractures in W–S and

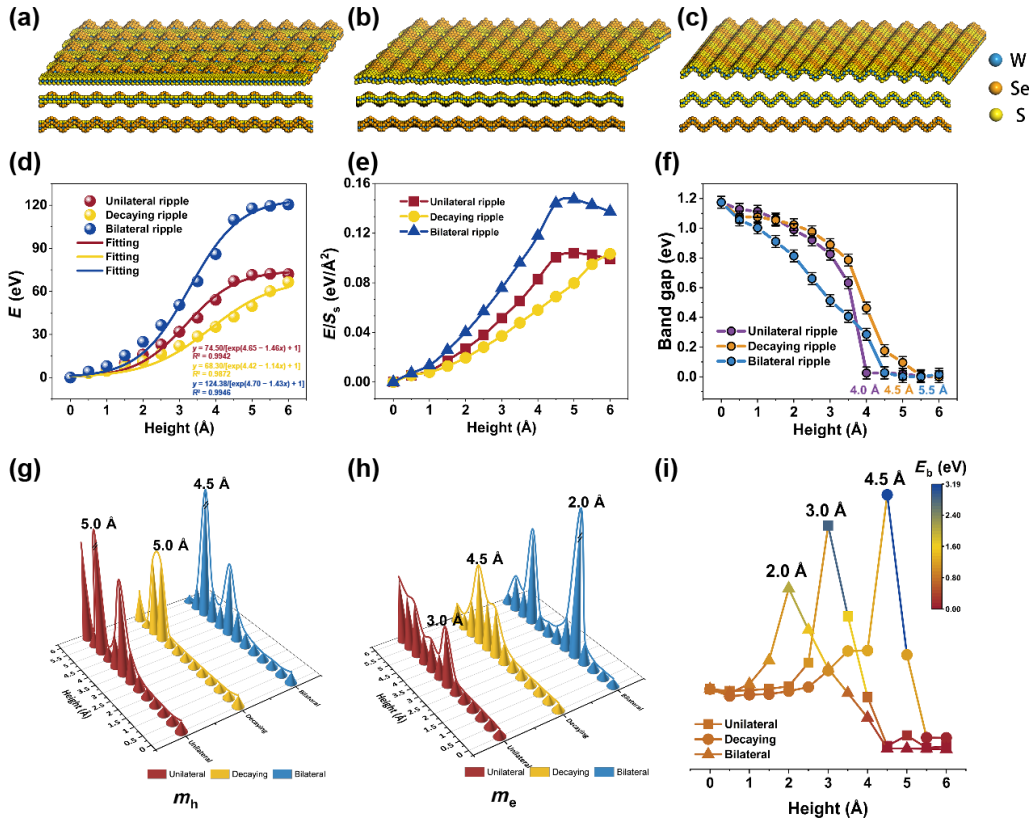

Figure 3 WS_2/WSe_2 lateral heterojunction structure and electronic properties. Structural demonstrations of (a) unilateral ripple, (b) decaying ripple, and (c) bilateral ripple. The (d) energy, (e) average energy, and (f) band gaps of the three heterojunctions. The effective mass of (g) electrons and (h) holes of the three heterojunctions. (i) The exciton binding energy estimated by three rippled heterojunctions.

W–Se bonds. Among the entire structure, the bilateral ripples showed the most severe bond length ruptures, indicating the highest overall structural strain. In the unilateral ripples, bond rupture at the interface was significantly stronger than in the other two structures, suggesting that the asymmetric unilateral structure experiences greater strain at the interface. In contrast, the decaying ripples had a markedly lower incidence of bond rupture, which gradually decreased with increasing ripple height (Fig. S5(b) in the ESM).

Furthermore, we statistically analyzed the bond lengths of W–S and W–Se in the upper and lower layer at the interface (Figs. S4(c) and S4(d) in the ESM). In both the unilateral and bilateral ripples, when the ripple height was within the range of 0 to 3.5 Å, the W–S bonds were primarily under tension, while the W–Se bonds were under slight tension. When the ripple height exceeded 3.5 Å, the upper layer W–S bonds at the crest of the ripples in the unilateral ripples were compressed, while the lower layer W–S bonds were under strong tension, with the opposite being true at the edges. Concurrently, the W–Se bonds experienced significant stretching and compression at the two waists of the ripples. When the ripple height was greater than 3.5 Å, the W–S bonds in the bilateral ripples were almost entirely compressed, with only slight tension at the crest. The changes in W–Se bond length were similar to those in the unilateral ripples. The decaying ripples, however, showed a slightly stretched state for W–S bonds, and the changes in W–Se bond length were significantly smaller than in the other two structures. In summary, our research has detailedly revealed the impact of ripple strain on bond length and bond rupture behavior in heterojunctions. These findings provide important insights into the local strain distribution within heterojunctions and its effects on the structural and electronic properties of the materials. These observations highlight the potential of ripple structures in modulating the electronic and mechanical properties of two-dimensional materials and offer valuable guidance for the design of new heterojunction devices.

The energies of these types of three rippled heterojunctions have been compared, which all the similar trends as the "Fermi-like distribution" of energy (Fig. 3(d)). For the same ripple height, the ripple energy shows an order as D-Ripple < U-Ripple < B-Ripple, indicating that stronger ripples largely increase the heterojunction energy. It is noted that the energy of both the U-Ripple and B-Ripple reaches stable when the ripple height achieves 4.5 Å. In comparison, the D-Ripple shows a continuously increasing energy trend as the ripple height increases. Meanwhile, the average energies of the U-Ripple and B-Ripple show a volcanic trend and the threshold is 4.5 Å (Fig. 3(e)). The average energy also shows the energy order as D-Ripple < U-Ripple < B-Ripple at the same ripple height. The energy comparisons indicate that the D-Ripple has the lowest energy with the highest stability, which is attributed to the lowest strain. However, the D-Ripple displays a monotonically increasing trend as the ripple height increases. This indicates that with the presence of large ripples in the D-Ripple structure, the average energy will potentially exceed other types of ripples, which is observed at the ripple height of 6.0 Å.

Then, the electronic structures are investigated, where the D-Ripple, U-Ripple, and B-Ripple exhibit a gradually increasing metallization threshold at the ripple height of 4.0, 5.0, and 5.5 Å, respectively (Fig. 3(f)). The D-Ripple structure has the slowest band

gap decay, which is potentially ascribed to the largest space to alleviate the influence of strain on the electronic structures. With the increase of ripple height, the band structure of U-Ripple remains indirect band gap (Fig. S6(a) in the ESM) while D-Ripple and B-Ripple change from indirect to direct band gap at 3.5 and 2.5 Å, respectively (Figs. S6(b) and S6(c) in the ESM). In addition, the k-point positions in U-Ripple and D-Ripple remain unchanged between 0–3.0 Å. The DOSs of the three structures are further demonstrated, in which the DOSs of the D-Ripple show the smallest changes (Figs. S7–S9 in the ESM). This further confirms the smallest strain in the D-Ripple with the least affected electronic structures, which is consistent with the comparison of evolution trends in energies and band structures among different ripples.

Beyond the electronic properties, the behaviors of free charge carriers are also explored through the estimations of the effective mass (Figs. 3(g) and 3(h)). From 3.0 Å, the effective mass of electrons and holes begins to change. This is supportive of the band structure evolutions, where the CBM/VBM becomes flattened with a sharp reduction in the band gap after 3.0 Å (Figs. 2(a)–2(c) and 3(f)). The highest effective mass of electrons corresponds to the three structures with ripple heights of 2.0, 4.5 and 3.0 Å, respectively. In comparison, the highest hole effective mass is reached at higher ripple heights for the three structures of 5.0, 4.5 and 5.0 Å, respectively. These results unravel that less stable rippled structures are easier to activate the fast transportations of free charge carriers. More importantly, the exciton binding energy E_b (Fig. 3(i)) [39, 40] calculation formula is as follows (Eq. (11))

$$E_b^{ex} = \frac{4 \times 13.6 \mu_{ex}}{m_e \varepsilon_s^2} \tag{11}$$

where μ_{ex} is the effective exciton mass, $\mu_{ex} = \frac{m_e \times m_h}{m_e + m_h}$ and ε_s is the static dielectric constant of the materials calculated by optical properties. The formula reflects the relationship between the exciton binding energy and the effective masses of electrons and holes in the material, as well as the static dielectric constant of the crystal. Here, 13.6 eV is the binding energy of an electron in the $n = 1$ orbit of a hydrogen atom, which is used as a proportionality factor to calculate the exciton binding energy. The factor of 4 accounts for the motion of excitons in three-dimensional space and the shielding effect of the crystal on the Coulomb interaction. This model is applicable when the radius of the exciton is much larger than the lattice constant, resulting in the formation of Wannier excitons, which can be simulated using a hydrogen-like model. Notably, the exciton binding energy displays volcano trends, where the U-Ripple, D-Ripple, and B-Ripple exhibit the highest binding energy at 5.0, 4.5, and 5.0 Å, respectively. By controlling the ripple morphology, the exciton binding energy can be maximized to optimize the optoelectronic properties of the heterostructure materials. Since the effective mass of the electron has the same peak positions as the exciton binding energy, indicating that the exciton binding energy of the three lateral heterojunction structures is dominated by the effective mass of the electron. Excitonic properties in heterojunctions of monolayer TMDCs are correlated with band offset and the Coulomb interaction between electrons and holes [41–43]. Our study further reveals that modulating the ripple structure within these heterojunctions allows for the tuning of exciton binding energies and the control of the overlap between electron and hole wave functions, thereby enhancing the optoelectronic performance of the materials. This discovery not only confirms the findings of Lau et al. [44]. but also provides novel strategies for the design of TMD-based optoelectronic devices.

To enable the applications of TMDCs in optoelectronic devices, the optical properties are equally important as the electronic structures, which are related to varying material properties. The simulated absorption spectra of the three structures in the blue-violet region of 400–470 nm show a volcanic trend (Figs. 4(a)–4(c)). The absorption peak of the D-Ripple decreases uniformly in this region while the absorption peak of the B-Ripple decreases more sharply. Starting from the ripple height of 2.5 Å, the absorption intensity of U-Ripple and B-Ripple increased significantly in the range of 600–800 nm, which is over 3 times higher than the flat heterojunction without any ripples. In contrast, the absorption intensity of D-Ripple only reaches two times increases relative to the flat heterojunction. Based on such results, we can flexibly modulate the optical absorption of a specific range by precisely designing a rippled strain structure in optoelectronic devices. Further detailed investigations of the dielectric functions are performed, which is one of the key parameters to determine the responses of TMDCs to the external electric field. The main difference in the real part (ε_1) of the dielectric functions is located in the range of 0–3 eV while the excitation photon energy is in the range of 0.8–1.7 eV (Fig. 4(d)). It is noted that ε_1 of B-Ripple with a ripple height of 5.0–6.0 Å has negative regions, which leads to poor responses to the external electric fields with a negative refractive index that cannot support the light propagation. The static dielectric constant shows a parallel increase with the ripple height, which is supportive of the increasing in-plane polarization (Fig. S10(a) in the ESM). Notably, the static dielectric constants of three different heterojunctions are similar when the ripple height is smaller than 4 Å. When the ripple height exceeds 4 Å, a drastic increase in the static dielectric constants is noticed, especially the B-Ripple. The work functions of the heterojunction keep decreasing as the ripple height increases, revealing that the formation of large ripples is beneficial for electron transfer from the heterojunction surfaces (Fig. S10(b) in the ESM). Meanwhile, the imaginary part (ε_2) of the dielectric function reflects the absorption characteristics of the material to light (Fig. 4(e)). As the ripple height increases, we notice the main peaks of ε_2 gradually shift towards smaller energy, revealing that the bonding conditions of heterojunctions have been changed. From the ripple height of 4.5 Å, the main peaks of ε_2 have been shifted to 0–2.0 eV with significantly enlarged values in an order of B-Ripple > U-Ripple > D-Ripple. The change of the ε_2 indicates the enhanced absorption of light and electron transition within 0–2 eV and induces the energy loss of light, which is consistent with the trend in the absorption spectrum [44, 45].

The polarization effect has also been studied by the correlation energy, which gradually changes from negative to positive as the ripple heights (Fig. S11 in the ESM). The orbital analysis shows that the electron near E_F is driven by strain to accumulate at the WSe_2 ripple side in the U-Ripples and D-Ripples, where stronger d-p-d orbital coupling is formed on the WSe_2 side of the D-Ripple (Figs. S12–S14 in the ESM). For the B-Ripple, the electronic distributions are located relatively even on both sides of the heterojunction. These results confirm the formation of the in-plane electric field with charge separation and locking, which leads to the gradually enlarging in-plane polarization. Meanwhile, the Hirshfled population analysis (HPA) of the three rippled heterojunctions further confirms the increasing in-plane electric fields on both sides of the heterojunction, which agrees well with the static dielectric constant results (Figs. S15–S17 in the ESM). In addition, the

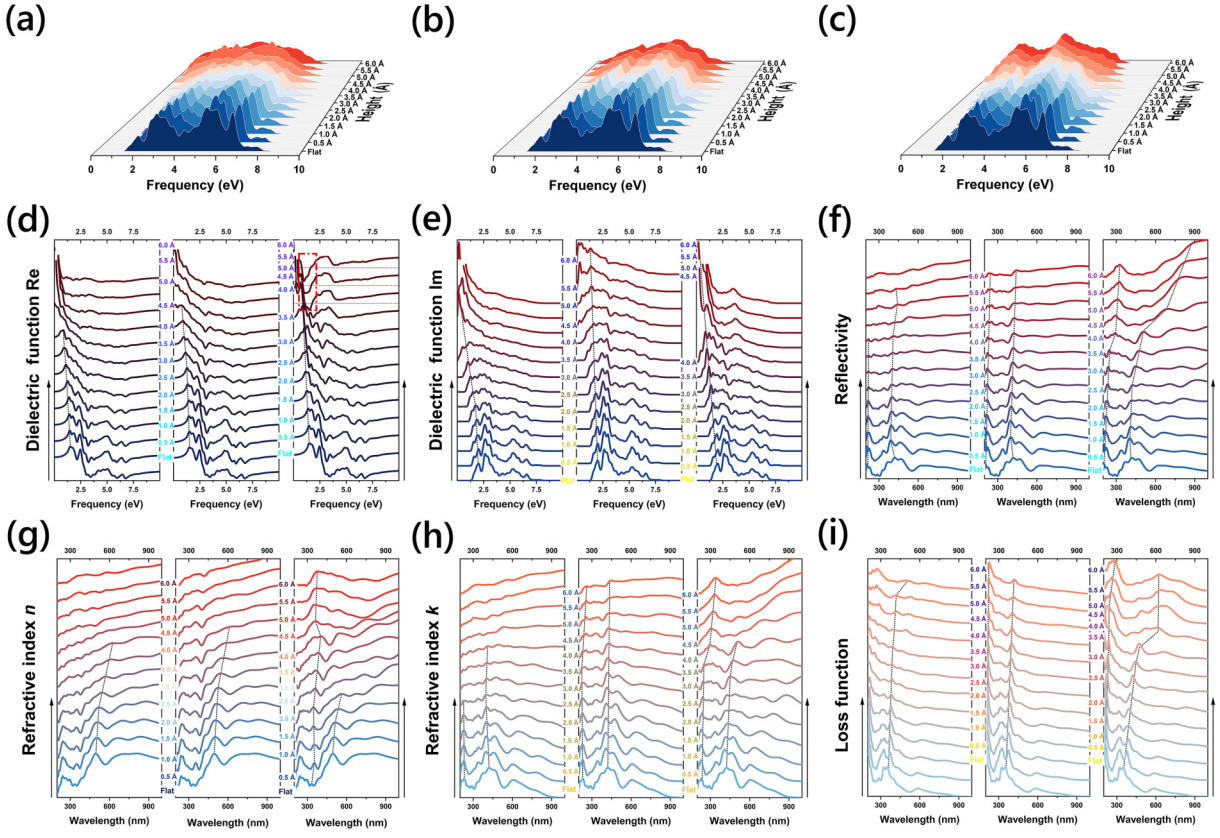

Figure 4 Optical properties of three heterojunctions. Absorption spectra of heterojunctions with (a) unilateral ripple, (b) decaying ripple, and (c) bilateral ripple. The (d) real part (Re) and (e) imaginary part (Im) of the dielectric function of the three rippled heterojunctions. (f) Reflection spectra of three rippled heterojunctions. (g) Real part (n) and (h) imaginary part (k) of the refractive index of the three rippled heterojunctions. (i) Energy loss spectra of three rippled heterojunctions. For (d)–(i), the left, middle, and right panels are the unilateral, decaying and bilateral ripple, respectively.

heterojunction will break into three parts by the ripples including ripples and the two side structures. Such structural fractures are consistent with the electron density difference (EDD) results at the ripple height of 4.5 Å (Figs. S18 and S19 in the ESM).

For the reflection spectrum, the position of the reflection peaks in the heterojunction is similar to the absorption peaks (Fig. 4(f)). Compared with the absorption spectra in Figs. 4(a)–4(c), the positions of the reflection peaks are close to the absorption peaks. As the ripple heights increase with stronger strains, the reflection peaks shift to higher wavelengths with lower energy, which is consistent with previous experiments that higher strains result in the lowering of the exciton energy [46, 47]. From 1.5 Å, the reflection of the three types of heterojunctions between 250–375 nm is significantly enhanced. There is a volcanic trend growth in the range of 375–550 nm, and the height of the turning point ripple is 0.5 Å, which can be reduced by up to 1 time. From 600 nm, all the heterojunctions show obvious reflection enhancement, reaching maximum enhancement factors are 4, 2, and 7 for U-Ripple, D-Ripple, and B-Ripple, respectively. The reflection coefficients of all the rippled heterojunctions exhibit converse trends with the increases of the ripple heights. The reflection coefficients of all systems decrease greatly in the visible range and then increase slightly after a wavelength of 550 nm. The reflection peak of different ripple systems is all located at 400 nm of visible light, indicating that all systems have more sensitive light reflection properties at this wavelength. For the real part (n) of the refractive index, the refractive index of all rippled heterojunctions is smaller than that of the flat structure in the visible light range, indicating that the formation of ripples in the heterojunction reduces the scattering of light (Fig. 4(g)). The refractive peaks of all systems correspond to the position of 500 nm, which gradually redshifts from 4.0 (U-Ripples), 4.5 (D-Ripples) and 2.5 Å (B-Ripples), respectively, which potentially modulates the phase of the light. On the other side, the imaginary part (k) determines the absorption process of light in the TMDCs, corresponding to the modulation of the light amplitude (Fig. 4(h)). Notably, the peak intensity is still strongly affected by the ripple height while the peak shifting has been strongly alleviated, especially for the D-Ripple. For both B-Ripples and U-Ripples, the peaks become less obvious and have been blurred by the intensity increases. These results demonstrate that ripple control is not guaranteed to modulate optical signals by changing the real and imaginary parts of the refractive index of TMDCs. This finding is important for the development of hybrid fiber modulators or other advanced optical devices. The extinction coefficient is also revealed by the imaginary part of the refractive index, which shows similar trends to the reflectivity (Fig. 4(i)). The peak position of all systems in the light range is 400 nm and the extinction coefficient decreases first and then increases at 500 nm with the increasing height of the ripple. For the energy loss function of the heterojunction, all the rippled heterojunctions also display a decrease first and then an increase in the visible light range. The peaks of the three heterojunctions at 400 nm gradually redshift to 450 nm and decrease with the increase of the ripple height. At the same ripple height, the energy loss in the D-Ripple is the lowest, and the energy loss in the B-Ripple is the highest, revealing that the strain will increase the energy loss when the electrons transfer through the material. It has been demonstrated that interfacial

strain significantly influences the optical properties of heterojunctions [48, 49]. Specifically, the introduction of compressive strain can realign the energy band structure at the heterojunction interface, thereby enhancing the separation efficiency and transport capability of photogenerated electron-hole pairs, which in turn significantly improves the photocurrent and photoresponsivity of photodiodes. The findings of this study reveal that strain engineering is an effective approach to optimize the optoelectronic performance of two-dimensional materials, providing crucial guidance for the development of new types of flexible optoelectronic devices.

Besides the electronic structures and optical properties, we further evaluate the phonon properties of the rippled heterojunctions through the phonon DOS (Figs. 5(a)–5(c)). The phonon PDOS indicates the acoustic and optical branches are mainly contributed by the W atom vibration and the S/Se anion vibration, respectively. For the flat heterojunction, we notice that there is not an evident gap between the acoustic and optical branches, which is ascribed to the coupling at the heterojunction interface. With the introduction of ripples, the peak that appears at 0 cm^{-1} is noted for all the phonon DOS, which belong to the acoustic mode and are potentially ascribed to the fixed W atoms during optimizations. Compared to the flat heterojunction, the imaginary frequency in the rippled structures is slightly increased, which indicates that enlarged strain further breaks the dynamical stability of the monolayer structure [50]. The low-frequency optical branches are more sensitive to the ripple-induced strain, which is mainly located in the range between 100–150 cm^{-1} due to the vibration of anions at the interface. As the height of the ripples increases, we observe that the vibration contribution of S gradually decreases until it approaches a similar level with Se. Notably, the peak of the phonon TDOSs of the three heterojunction structures decreases in the range of 250–330 cm^{-1} with broadened splitting peaks, revealing the local bonding changes under the strains. The broadening of the phonon DOS means that the ripple strain causes more phonon states to be generated in the heterojunction, which is able to realize the modulations of thermal conductivity flexibly. For the U-Ripples, the TDOSs gradually split from a single peak to multiple peaks at 1.5 Å and then re-degenerate to a single peak at 4.5 Å (Fig. 5(a)). Similar broadening of TDOSs is also noted for D-Ripples and B-Ripples, supporting that the ripple strain affects the coupling between anions in the material as well as the sensitivity of the optical branch (Figs. 5(b) and 5(c)). In the low-frequency region of 150 cm^{-1}, the phonon DOS also becomes broadened and gradually disappears as the ripple is introduced. Since the low-frequency phonon state is closely related to the acoustic branch as the main contributor to the thermal conductivity, the reduction of the phonon states leads to the decrease of the thermal conductivity of these three rippled structures. The new phonon states induced by the ripples result in an increase in phonon scattering, which reduces the mean free path of phonons.

In the study of two-dimensional van der Waals (vdW) materials, the low-dimensional structure and reduced electrostatic screening effects together lead to a significant enhancement of exciton-phonon coupling. Particularly, transition metal dichalcogenides (TMDCs), with their unique valley polarization and spin-orbit coupling, offer a diverse range of ways to modulate electron-phonon coupling, making them an ideal platform for investigating electron-phonon interactions [51]. Within these materials, the strengthened exciton-phonon coupling facilitates the capture of

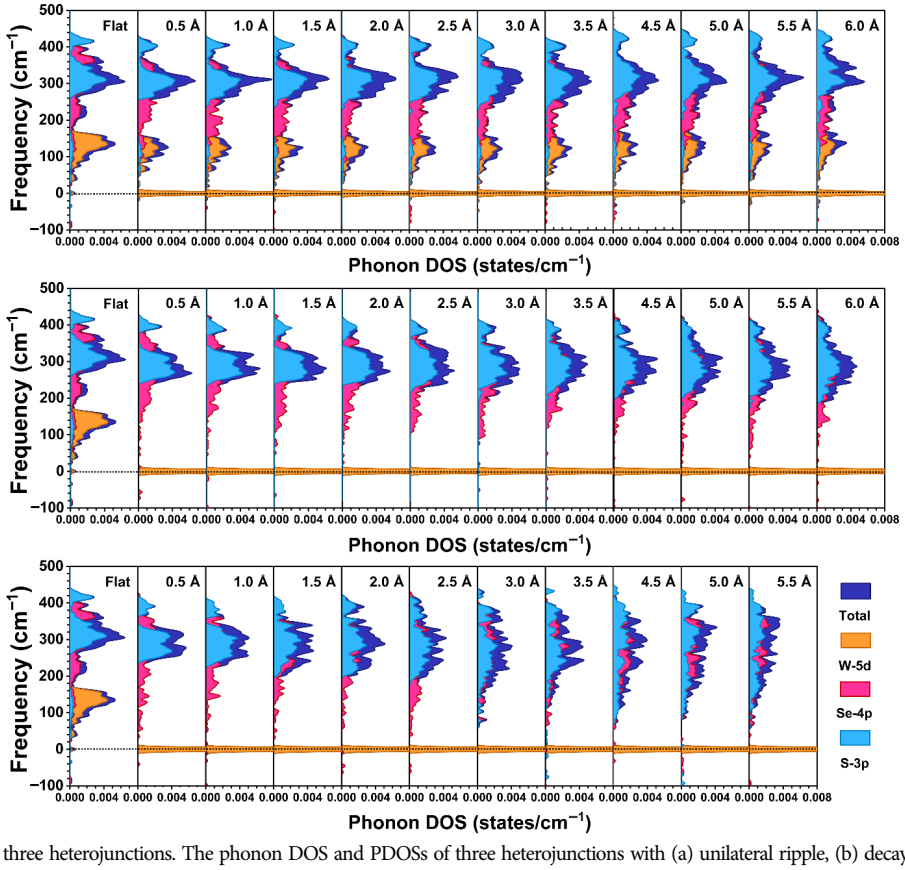

Figure 5 Phonon DOS of three heterojunctions. The phonon DOS and PDOSs of three heterojunctions with (a) unilateral ripple, (b) decaying ripple, and (c) bilateral ripple, respectively.

excited electron-hole pairs by the lattice's deformation potential, leading to the formation of self-trapped excitons (STEs). These STEs are more stable due to their association with lattice distortions. In our research, we observed that as the height of the ripples increases, the strain broadens the phonon density of states, providing more scattering opportunities for electrons and thus enhancing electron-phonon coupling. Additionally, the increased lattice disorder offers more scattering centers for electrons, further intensifying the interaction between electrons and phonons. With increasing lattice distortion, the exciton binding energy exhibits a volcanic trend of increase, indicating that within a certain range of ripple heights, strong electron-phonon coupling promotes the formation and stability of self-trapped excitons. However, when the strain increases further, disrupting the lattice's periodicity and integrity, the stability of self-trapped excitons is reduced, manifesting as a decrease in exciton binding energy. Therefore, through strain engineering, we can effectively control electron-phonon coupling, thereby modulating the electronic and optical properties of semiconductor materials to meet specific application requirements. This control offers new approaches and methods for the design of novel optoelectronic devices.

The heat capacity of the three heterojunction structures also decreases with the increase of the internal stress of the material, resulting in a decrease in thermal conductivity, especially for D-Ripples and B-Ripples (Fig. S20 in the ESM). This reduction in heat capacity adversely affects the thermal conductivity of the material towards the decreasing trend, which is consistent with the phonon DOS results. Such a correlation between heat capacity and thermal conductivity provides a key insight into our understanding of the thermal transport properties of materials under different stress states. On the other hand, if the broadening of the phonon DOS is accompanied by the increase of phonon group velocity, the thermal conductivity is improved. Zhang et al. [4] have confirmed that the thermal rectification effect of the nanoscale interface in the heterojunction effectively enhanced thermal conductivity. Accordingly, by controlling the ripples precisely in the heterojunction, novel thermal conductive materials are able to be achieved in the future. In contrast, the low-frequency optical branch changes in D-Ripples and B-Ripples are different from that in U-Ripples. The peaks in the low-frequency optical branches are largely weakened with ripple formation in D-Ripples and B-Ripples, which is attributed to the co-existence of both energy upconversion and downconversion contributed by the vibrations of Se and S atoms, respectively. These opposite phonon peak trends indicate the energy transfer from Se to S atoms, which largely change the vibration modes at the heterojunction faces. These results demonstrate that the interface anion coupling plays a key role in modulating the thermal conductivity of the materials. This research direction not only enriches the understanding of the thermal rectification effect but also opens up new possibilities for the development of thermal management technology.

3 Conclusions

In this work, we have carried out theoretical explorations on the formation and dynamic processes of ripples in representative TMDCs and heterojunctions. Through detailed analysis, we have classified the two stages of ripple formation including the elastic strain and fracture threshold by successfully identifying the correlations between thermodynamic stability and ripple height, enabling accurate guidance to optimize the properties of TMDCs. Through detailed electronic structure analysis, the strain-driven charge carrier transfer phenomenon has been identified to explain the ripple-induced electronic modulations, where the highly electroactive electrons near the E_F gradually accumulated at the top of the ripples, inducing a strong polarization in TMDCs. More importantly, the lateral heterojunctions with the three most possible ripple conditions (U-Ripples, D-Ripples, and B-Ripples) have been compared regarding the electronic optical and phonon properties. In particular, the larger strain in B-Ripples dominated by strong d-p-d orbital couplings leads to a stronger trend towards metallization, improved electron transfer capability, and enhanced electron-dominated in-plane polarization effect. For different optical properties, we notice that the strain levels determined by the ripples do not affect the overall peak positions and turning points in different optical properties, and only their sensitivity to ripple heights is modulated. The further phonon DOS results not only reveal that the optical branches dominated by anions are more sensitive but also show that the control of ripples is beneficial to developing novel thermal conductive materials. Therefore, for the commonly observed ripples in 2D materials, this work has provided significant insights into their formation and impacts on thermodynamic, electronic, and optical properties, opening the possibilities of developing novel luminescence, optoelectronic, and even thermal conductive materials by precise morphology controls in the future.

4 Calculation method

In this paper, the first-principles calculation is based on the CASTEP program [52]. In the calculation, the generalized gradient approximation (GGA) and Perdew–Burke–Ernzerhof (PBE) are used to accurately reveal the interaction of electron exchange-correlation energy [53–55]. The calculations are performed using ultrafine quality and ultra-soft pseudopotential. Based on the convergence test. The cutoff energy is 380 eV. The Broyden–Fletcher–Goldfarb–Shannon (BFGS) algorithm is used to achieve energy minimization [56, 57]. In the process of structural optimization, the standard is set as: the Hellmann–Feynman forces should be less than 0.001 eV/Å; the total energy should not exceed 5×10^{-5} eV per atom.

To construct the models, we have considered the ripple structure in the armchair and zigzag directions with the monolayer ripples, which are called armchair ripples and zigzag ripples, respectively (Fig. S1 in the ESM). For all the ripple structures, the length and period change in two directions according to the ripple modeling function equations. As an example, we apply the following modeling function equations for periodic superlattice structural model building (Eqs. (12) and (13))

$$\text{Armchair ripple}: z = A\cos\left(\frac{2\pi x}{a}\right) \tag{12}$$

$$\text{Zigzag ripple}: z = B\cos\left(\frac{2\pi y}{b}\right) \tag{13}$$

where A and B are the amplitudes of the ripple function, and the ripple heights are $2A$ and $2B$, respectively. The ripple heights of different size supercells are different, but all the ripple heights are in the range of 0–7 Å, with 0.5 Å as an increasing step for the ripple height. In the equation, a and b are the length and width of the supercell, which also represent the periods in armchair and zigzag directions, respectively. In order to study the properties of TMDCs materials, we have selected three monolayer TMDCs including

MoS_2, WS_2, and WSe_2 to build up the ripple structures. For the structures in this work, we have named them by the supercell size, which is $3 \times N$ (N = 4, 5, 6, 7, 8, 9) and $N \times 5$ (N = 2, 3, 4, 5, 6), respectively.

Electronic Supplementary Material: Supplementary material (ripple structure demonstrations, electronic analysis of ripple structures, fitting of elastic strain stage, correlation energy, and energy fitting parameter analysis, etc.) is available in the online version of this article at https://doi.org/10.26599/NR.2025.94907091.

Data availability

All data needed to support the conclusions in the paper are presented in the manuscript and the ESM. Additional data related to this paper may be requested from the corresponding author upon request.

Acknowledgements

The authors gratefully acknowledge the support from Research Grant Council of Hong Kong (No. 15304023), National Natural Science Foundation of China/Research Grant Council of Hong Kong Joint Research Scheme (No. N_PolyU502/21), the funding for Projects of Strategic Importance of The Hong Kong Polytechnic University (No. 1-ZE2V), Shenzhen Fundamental Research Scheme-General Program (No. JCYJ20220531090807017), and Natural Science Foundation of Guangdong Province (No. 2023A1515012219). The authors also thank the support from Research Centre for Carbon-Strategic Catalysis (RC-CSC), Research Institute for Smart Energy (RISE), and Research Institute for Intelligent Wearable Systems (RI-IWEAR) of the Hong Kong Polytechnic University.

Declaration of competing interest

All the contributing authors report no conflict of interests in this work. Author Zhong Lin Wang is the advisory board member of this journal, but he is not involved in the peer-review or decision of this article.

Author contribution statement

H. T. Y.: Calculation design, data curation and analysis, writing manuscript. M. Z. S.: Data analysis, writing manuscript. X. W., Z. G. X., J. H. K. and S. P. L.: Data analysis. B. L. H.: Project administration, funding acquisition, writing manuscript, calculation design, data analysis. Z. L. W.: Project administration, funding acquisition. All the authors have approved the final manuscript.

Use of AI statement

None.

References

[1] Novoselov, K. S.; Geim, A. K.; Morozov, S. V.; Jiang, D.; Zhang, Y.; Dubonos, S. V.; Grigorieva, I. V.; Firsov, A. A. Electric field effect in atomically thin carbon films. *Science* **2004**, *306*, 666–669.

[2] Wang, X. M.; Lan, S. F. Optical properties of black phosphorus. *Adv. Opt. Photonics* **2016**, *8*, 618–655.

[3] Wei, Y.; Zhang, P.; Soomro, R. A.; Zhu, Q. Z.; Xu, B. Advances in the synthesis of 2D MXenes. *Adv. Mater.* **2021**, *33*, 2103147.

[4] Zhang, Y. F.; Lv, Q.; Wang, H. D.; Zhao, S. Y.; Xiong, Q. H.; Lv, R. T.; Zhang, X. Simultaneous electrical and thermal rectification in a monolayer lateral heterojunction. *Science* **2022**, *378*, 169–175.

[5] Pandey, M.; Pandey, C.; Ahuja, R.; Kumar, R. Straining techniques for strain engineering of 2D materials towards flexible straintronic applications. *Nano Energy* **2023**, *109*, 108278.

[6] Wada, N.; Pu, J.; Takaguchi, Y.; Zhang, W. J.; Liu, Z.; Endo, T.; Irisawa, T.; Matsuda, K.; Miyauchi, Y.; Takenobu, T. et al. Efficient and chiral electroluminescence from in-plane heterostructure of transition metal dichalcogenide monolayers. *Adv. Funct. Mater.* **2022**, *32*, 2203602.

[7] Zhang, Z. W.; Huang, Z. W.; Li, J.; Wang, D.; Lin, Y.; Yang, X. D.; Liu, H.; Liu, S.; Wang, Y. L.; Li, B. et al. Endoepitaxial growth of monolayer mosaic heterostructures. *Nat. Nanotechnol.* **2022**, *17*, 493–499.

[8] Zhu, J. T.; Li, W.; Huang, R.; Ma, L.; Sun, H. M.; Choi, J. H.; Zhang, L. Q.; Cui, Y.; Zou, G. F. One-pot selective epitaxial growth of large WS_2/MoS_2 lateral and vertical heterostructures. *J. Am. Chem. Soc.* **2020**, *142*, 16276–16284.

[9] Pomerantseva, E.; Gogotsi, Y. Two-dimensional heterostructures for energy storage. *Nat. Energy* **2017**, *2*, 17089.

[10] Rhodes, D.; Chae, S. H.; Ribeiro-Palau, R.; Hone, J. Disorder in van der Waals heterostructures of 2D materials. *Nat. Mater.* **2019**, *18*, 541–549.

[11] Duan, X. D.; Wang, C.; Shaw, J. C.; Cheng, R.; Chen, Y.; Li, H. L.; Wu, X. P.; Tang, Y.; Zhang, Q. L.; Pan, A. L. et al. Lateral epitaxial growth of two-dimensional layered semiconductor heterojunctions. *Nat. Nanotechnol.* **2014**, *9*, 1024–1030.

[12] Han, Y. M.; Nguyen, K.; Cao, M.; Cueva, P.; Xie, S. E.; Tate, M. W.; Purohit, P.; Gruner, S. M.; Park, J.; Muller, D. A. Strain mapping of two-dimensional heterostructures with subpicometer precision. *Nano Lett.* **2018**, *18*, 3746–3751.

[13] Zhou, W.; Zhang, Y. Y.; Chen, J. Y.; Li, D. D.; Zhou, J. D.; Liu, Z.; Chisholm, M. F.; Pantelides, S. T.; Loh, K. P. Dislocation-driven growth of two-dimensional lateral quantum-well superlattices. *Sci. Adv.* **2018**, *4*, eaap9096.

[14] Wang, Y. N.; Gao, X.; Yang, K. N.; Gu, P. F.; Lu, X.; Zhang, S. H.; Gao, Y. C.; Ren, N. J.; Dong, B. J.; Jiang, Y. H. et al. Quantum Hall phase in graphene engineered by interfacial charge coupling. *Nat. Nanotechnol.* **2022**, *17*, 1272–1279.

[15] He, Q. L.; Liu, H. C.; He, M. Q.; Lai, Y. H.; He, H. T.; Wang, G.; Law, K. T.; Lortz, R.; Wang, J. N.; Sou, I. K. Two-dimensional superconductivity at the interface of a Bi_2Te_3/FeTe heterostructure. *Nat. Commun.* **2014**, *5*, 4247.

[16] Gibertini, M.; Koperski, M.; Morpurgo, A. F.; Novoselov, K. S. Magnetic 2D materials and heterostructures. *Nat. Nanotechnol.* **2019**, *14*, 408–419.

[17] Novoselov, K. S.; Mishchenko, A.; Carvalho, A.; Castro Neto, A. H. 2D materials and van der Waals heterostructures. *Science* **2016**, *353*, aac9439.

[18] Xie, S. E.; Tu, L. J.; Han, Y. M.; Huang, L. J.; Kang, K.; Lao, K. U.; Poddar, P.; Park, C.; Muller, D. A.; DiStasio, R. A. Jr. et al. Coherent, atomically thin transition-metal dichalcogenide superlattices with engineered strain. *Science* **2018**, *359*, 1131–1136.

[19] Tian, X. Z.; Yan, X. X.; Varnavides, G.; Yuan, Y. K.; Kim, D. S.; Ciccarino, C. J.; Anikeeva, P.; Li, M. Y.; Li, L. J.; Narang, P. et al. Capturing 3D atomic defects and phonon localization at the 2D heterostructure interface. *Sci. Adv.* **2021**, *7*, eabi6699.

[20] Tian, X. Z.; Kim, D. S.; Yang, S. Z.; Ciccarino, C. J.; Gong, Y. J.; Yang, Y.; Yang, Y.; Duschatko, B.; Yuan, Y. K.; Ajayan, P. M. et al. Correlating the three-dimensional atomic defects and electronic properties of two-dimensional transition metal dichalcogenides. *Nat. Mater.* **2020**, *19*, 867–873.

[21] Herbig, C.; Zhang, C. X.; Mujid, F.; Xie, S. E.; Pedramrazi, Z.; Park, J.; Crommie, M. F. Local electronic properties of coherent single-layer WS_2/WSe_2 lateral heterostructures. *Nano Lett.* **2021**, *21*, 2363–2369.

[22] Sun, Y. G.; Choi, W. M.; Jiang, H. Q.; Huang, Y. Y.; Rogers, J. A.

Controlled buckling of semiconductor nanoribbons for stretchable electronics. *Nat. Nanotechnol.* **2006**, *1*, 201–207.
[23] Zhong, Y.; Zhang, L. N.; Park, J. H.; Cruz, S.; Li, L.; Guo, L.; Kong, J.; Wang, E. N. A unified approach and descriptor for the thermal expansion of two-dimensional transition metal dichalcogenide monolayers. *Sci. Adv.* **2022**, *8*, eabo3783.
[24] Kum, H.; Lee, D.; Kong, W.; Kim, H.; Park, Y.; Kim, Y.; Baek, Y.; Bae, S. H.; Lee, K.; Kim, J. Epitaxial growth and layer-transfer techniques for heterogeneous integration of materials for electronic and photonic devices. *Nat. Electron.* **2019**, *2*, 439–450.
[25] Sun, M. Z.; Wu, T.; Huang, B. L. Anion charge density disturbance induces in-plane instabilities within 2D lateral heterojunction of TMD: An atomic view. *Nano Energy* **2020**, *70*, 104484.
[26] Zhang, Z. W.; Chen, P.; Duan, X. D.; Zang, K. T.; Luo, J.; Duan, X. F. Robust epitaxial growth of two-dimensional heterostructures, multiheterostructures, and superlattices. *Science* **2017**, *357*, 788–792.
[27] Li, J.; Yang, X. D.; Liu, Y.; Huang, B. L.; Wu, R. X.; Zhang, Z. W.; Zhao, B.; Ma, H. F.; Dang, W. Q.; Wei, Z. et al. General synthesis of two-dimensional van der Waals heterostructure arrays. *Nature* **2020**, *579*, 368–374.
[28] Zhang, C. D.; Li, M. Y.; Tersoff, J.; Han, Y. M.; Su, Y. S.; Li, L. J.; Muller, D. A.; Shih, C. K. Strain distributions and their influence on electronic structures of WSe_2–MoS_2 laterally strained heterojunctions. *Nat. Nanotechnol.* **2018**, *13*, 152–158.
[29] Ghosh, R.; Papnai, B.; Chen, Y. S.; Yadav, K.; Sankar, R.; Hsieh, Y. P.; Hofmann, M.; Chen, Y. F. Exciton manipulation for enhancing photoelectrochemical hydrogen evolution reaction in wrinkled 2D heterostructures. *Adv. Mater.* **2023**, *35*, 2210746.
[30] Li, M. Y.; Shi, Y. M.; Cheng, C. C.; Lu, L. S.; Lin, Y. C.; Tang, H. L.; Tsai, M. L.; Chu, C. W.; Wei, K. H.; He, J. H. et al. Epitaxial growth of a monolayer WSe_2–MoS_2 lateral p-n junction with an atomically sharp interface. *Science* **2015**, *349*, 524–528.
[31] Chaurasiya, R.; Dixit, A.; Pandey, R. Strain-mediated stability and electronic properties of WS_2, Janus WSSe and WSe_2 monolayers. *Superlattices Microstruct.* **2018**, *122*, 268–279.
[32] Wang, F.; Li, S. H.; Bissett, M. A.; Kinloch, I. A.; Li, Z. L.; Young, R. J. Strain engineering in monolayer WS_2 and WS_2 nanocomposites. *2D Mater.* **2020**, *7*, 045022.
[33] Tang, M. C.; Zhang, D. Z.; Wang, D. Y.; Deng, J.; Kong, D. T.; Zhang, H. Performance prediction of 2D vertically stacked MoS_2–WS_2 heterostructures base on first-principles theory and Pearson correlation coefficient. *Appl. Surf. Sci.* **2022**, *596*, 153498.
[34] Yu, H. T.; Sun, M. Z.; Wu, X.; Chan, C. H.; Huang, B. L.; Wang, Z. L. Atomscopic of ripple origins for two-dimensional monolayer transition metal dichalcogenides. *Nano Res.* **2024**, *17*, 2136–2144.
[35] Li, J. L.; Duan, H. M.; Zeng, B. W.; Jing, Q.; Cao, B. B.; Chen, F. J.; Long, M. Q. Strain-induced band structure modulation in hexagonal boron phosphide/blue phosphorene vdW heterostructure. *J. Phys. Chem. C* **2018**, *122*, 26120–26129.
[36] Wu, T.; Sun, M. Z.; Huang, B. L. Probing the irregular lattice strain-induced electronic structure variations on late transition metals for boosting the electrocatalyst activity. *Small* **2020**, *16*, e2002434.
[37] Hu, S.; Lozada-Hidalgo, M.; Wang, F. C.; Mishchenko, A.; Schedin, F.; Nair, R. R.; Hill, E. W.; Boukhvalov, D. W.; Katsnelson, M. I.; Dryfe, R. A. et al. Proton transport through one-atom-thick crystals. *Nature* **2014**, *516*, 227–230.
[38] Wahab, O. J.; Daviddi, E.; Xin, B.; Sun, P. Z.; Griffin, E.; Colburn, A. W.; Barry, D.; Yagmurcukardes, M.; Peeters, F. M.; Geim, A. K. et al. Proton transport through nanoscale corrugations in two-dimensional crystals. *Nature* **2023**, *620*, 782–786.
[39] Kumar, A.; Ahluwalia, P. K. Mechanical strain dependent electronic and dielectric properties of two-dimensional honeycomb structures of MoX_2 (X = S, Se, Te). *Phys. B: Condens. Matter* **2013**, *419*, 66–75.
[40] Shi, D.; Guo, Z.; Bedford, N. 4-Semiconductor quantum dots. In *Nanomaterials and Devices*. Shi, D.; Guo, Z.; Bedford, N., Eds.; Elsevier: Amsterdam, 2015; pp 83–104.
[41] Lau, K. W.; Calvin; Gong, Z. R.; Yu, H. Y.; Yao, W. Interface excitons at lateral heterojunctions in monolayer semiconductors; *Phys. Rev. B* **2018**, *98*, 115427.
[42] Jiang, Y.; Chen, S. L.; Zheng, W. H.; Zheng, B. Y.; Pan, A. L. Interlayer exciton formation, relaxation, and transport in TMD van der Waals heterostructures. *Light: Sci. Appl.* **2021**, *10*, 72.
[43] Calman, E. V.; Fogler, M. M.; Butov, L. V.; Hu, S.; Mishchenko, A.; Geim, A. K. Indirect excitons in van der Waals heterostructures at room temperature. *Nat. Commun.* **2018**, *9*, 1895.
[44] Song, B. K.; Gu, H. G.; Fang, M. S.; Chen, X. G.; Jiang, H.; Wang, R. Y.; Zhai, T. Y.; Ho, Y. T.; Liu, S. Y. Layer-dependent dielectric function of wafer-scale 2D MoS_2. *Adv. Opt. Mater.* **2019**, *7*, 1801250.
[45] Tikuišis, K. K.; Dubroka, A.; Uhlířová, K.; Speck, F.; Seyller, T.; Losurdo, M.; Orlita, M.; Veis, M. Dielectric function of epitaxial quasi-freestanding monolayer graphene on Si-face 6H-SiC in a broad spectral range. *Phys. Rev. Mater.* **2023**, *7*, 044201.
[46] Carrascoso, F.; Li, H.; Obrero-Perez, J. M.; Aparicio, F. J.; Borras, A.; Island, J. O.; Barranco, A.; Castellanos-Gomez, A. Improved strain engineering of 2D materials by adamantane plasma polymer encapsulation. *npj 2D Mater. Appl.* **2023**, *7*, 24.
[47] Çakıroğlu, O.; Island, J. O.; Xie, Y.; Frisenda, R.; Castellanos-Gomez, A. An automated system for strain engineering and straintronics of 2D materials. *Adv. Mater. Technol.* **2023**, *8*, 2201091.
[48] Lin, P.; Zhu, L. P.; Li, D.; Xu, L.; Pan, C. F.; Wang, Z. L. Piezo-phototronic effect for enhanced flexible MoS_2/WSe_2 van der Waals photodiodes. *Adv. Funct. Mater.* **2018**, *28*, 1802849.
[49] Jiang, D. T.; Liu, Z. Y.; Xiao, Z.; Qian, Z. F.; Sun, Y. L.; Zeng, Z. Y.; Wang, R. H. Flexible electronics based on 2D transition metal dichalcogenides. *J. Mater. Chem. A* **2022**, *10*, 89–121.
[50] Sheng, H. H.; Long, H. X.; Zou, G. Z.; Bai, D. M.; Zhang, J. T.; Wang, J. L. Magnetic and phonon transport properties of two-dimensional room-temperature ferromagnet VSe_2. *J. Mater. Sci.* **2021**, *56*, 15844–15858.
[51] Lai, J. M.; Farooq, M. U.; Sun, Y. J.; Tan, P. H.; Zhang, J. Multiphonon process in Mn-doped ZnO nanowires. *Nano Lett.* **2022**, *22*, 5385–5391.
[52] Clark, S. J.; Segall, M. D.; Pickard, C. J.; Hasnip, P. J.; Probert, M. I. J.; Refson, K.; Payne, M. C. First principles methods using CASTEP. *Z. Kristallogr. Cryst. Mater.* **2005**, *220*, 567–570.
[53] Perdew, J. P.; Burke, K.; Ernzerhof, M. Generalized gradient approximation made simple. *Phys. Rev. Lett.* **1996**, *77*, 3865–3868.
[54] Hasnip, P. J.; Pickard, C. J. Electronic energy minimisation with ultrasoft pseudopotentials. *Comput. Phys. Commun.* **2006**, *174*, 24–29.
[55] Perdew, J. P.; Chevary, J. A.; Vosko, S. H.; Jackson, K. A.; Pederson, M. R.; Singh, D. J.; Fiolhais, C. Atoms, molecules, solids, and surfaces: Applications of the generalized gradient approximation for exchange and correlation. *Phys. Rev. B* **1992**, *46*, 6671–6687.
[56] Head, J. D.; Zerner, M. C. A broyden-fletcher-goldfarb-shanno optimization procedure for molecular geometries. *Chem. Phys. Lett.* **1985**, *122*, 264–270.
[57] Probert, M. I. J.; Payne, M. C. Improving the convergence of defect calculations in supercells: An *ab initio* study of the neutral silicon vacancy. *Phys. Rev. B* **2003**, *67*, 075204.